

Journal of Materials Chemistry A

Accepted Manuscript



This is an *Accepted Manuscript*, which has been through the Royal Society of Chemistry peer review process and has been accepted for publication.

Accepted Manuscripts are published online shortly after acceptance, before technical editing, formatting and proof reading. Using this free service, authors can make their results available to the community, in citable form, before we publish the edited article. We will replace this *Accepted Manuscript* with the edited and formatted *Advance Article* as soon as it is available.

You can find more information about *Accepted Manuscripts* in the [Information for Authors](#).

Please note that technical editing may introduce minor changes to the text and/or graphics, which may alter content. The journal's standard [Terms & Conditions](#) and the [Ethical guidelines](#) still apply. In no event shall the Royal Society of Chemistry be held responsible for any errors or omissions in this *Accepted Manuscript* or any consequences arising from the use of any information it contains.



Journal Name

ARTICLE

Synergistic effect of S,N-co-doped Mesoporous Carbon Materials with High Performance for Oxygen-Reduction Reaction and Li-ion Batteries

Received 00th January 20xx,
Accepted 00th January 20xx

DOI: 10.1039/x0xx00000x

www.rsc.org/

Gui-lin Zhuang,^{a,†} Jia-qi Bai,^{a,‡} Xin-yong Tao,^{b,‡} Jian-min Luo,^b Xin-de Wang,^a Yi-fen Gao,^a Xing Zhong,^a Xiao-nian Li,^a Jian-guo Wang^{*a}

S,N-co-doped porous carbon (SNPC) materials are good candidates for cathodic oxygen-reduction reaction (ORR) and lithium-ion batteries (LIBs). However, SNPC has low yield and high cost. Herein, we reported a new and efficient method of synthesizing S,N-co-doped mesoporous carbon material through the carbonization of S,N-containing precursors in molten ZnCl₂, where ZnCl₂ served as the ionic solvent and Lewis catalyst. The resultant SNPC-800 showed a mesoporous structure with a specific surface area of 1235 m²/g and mesopore-size range of 10-45 nm, which was considerably larger than those obtained through carbonization of ionic-liquid and fabrication of graphene oxides. Furthermore, ORR measurements exhibit good catalytic activity, comparable to the commercial Pt/C catalyst. Also the SNPC-800 material exhibited excellent good catalytic stability, and a high methanol tolerance compared to the commercial Pt/C catalyst. Density functional theory calculation results revealed that the catalytic property originated from the synergistic effect of S/N dopant and that the main catalytic reaction path followed an associative mechanism. LIB tests further showed high reversible capacity, as well as excellent cycling stability and rate performance.

Introduction

Research on the exploration of high-performance proton-exchange membrane fuel cells (PEMFCs) is largely stimulated by their wide-ranging potential applications¹. Generally, PEMFCs involve a reaction between a fuel at the anode and an oxidant (e.g. O₂) at the cathode using a catalyst to reduce electrochemical overpotential. In particular, electrocatalysts based on pure platinum and platinum-transition metal alloy are gaining considerable attention². However, given the low-kinetic characteristic of oxygen-reduction reaction³ (ORR), it usually requires a relatively high loading of precious Pt-based catalyst⁴. This requirement continues to hinder the extensive commercialization of fuel cells. Therefore, identifying a substitute for high-cost Pt catalysts is urgent.

The ordered matrix and unique electronic structure of heteroatom-doped porous carbon (PC) materials⁵ with high specific surface area and numerous active sites enable these materials to be ideal metal-free ORR catalysts. Since the report

of Jasinski on N-doped materials⁶, much effort has been devoted to investigate the controllable design of these materials. Notably, binary-doped PCs inherit individual electronic effect and generate synergistic effect on the catalytic reaction. Within this context, the nitrogen atom is regarded as the most effective dopant atom because of its electronegative property and odd-number electronic configuration⁷. And sulphur atom, featuring *p* orbitals in the outermost shell, possesses unique electronic structure similar with nitrogen atom but with different electronegativity⁸ and atomic radius, which is likely to induce structural defects in the matrix of PCs⁹. Consequently, one particular class of binary-doped cases featuring S, N dopants has received great interest because of its unique matching electronic structure of S and N atoms^{4b,10}. Traditional synthetic strategies of S, N-co-doped PC are concentrated on the thiourea-etching carbon materials and the carbonization of S,N-containing precursors, such as organic molecule^{10c} and ionic liquid¹⁰ⁱ, which have low yield and high-cost deficiency. Following catalytic design philosophy, these problems can be effectively resolved by using of catalyst. Molten ZnCl₂ at high temperature shows good solvents for S,N-containing azole and good catalytic activity for the trimerization reaction¹¹. Previously, A. Thomas et al. reported the synthesis of covalent organic frameworks by heating a mixture of nitrile and ZnCl₂¹¹. To date, the PC materials prepared by this method are still not reported.

Meanwhile, lithium-ion batteries (LIBs) are attracting tremendous attention because of their practical applications in electric vehicles, laptops, personal digital assistants, and

^a Institute of Industrial Catalysis, College of Chemical Engineering, Zhejiang University of Technology, Hangzhou, People's Republic of China, 310032.

^b College of Material Science and Engineering, Zhejiang University of Technology, Hangzhou, People's Republic of China, 310032.

[†] These authors contributed equally.

Electronic Supplementary Information (ESI) available: [SEM,TEM figure and structural characterization of NPC-800 and SPC-800; XPS pore distribution, TG curve and elemental analysis of SNPC; ORR and EIS result of SNPC, SPC and NPC; LIB property of SNPC-800, NPC-800 and SPC-800; DFT calculation result of ORR mechanism for SNPC-800.]. See DOI: 10.1039/x0xx00000x

cellular phone¹². High energy and high-power densities are prerequisites for the high-performance applications of LIBs¹³. However, to obtain LIBs with high-power densities is still a great challenge because of the kinetic problems of the electrode materials^{12c}. Generally, high-rate ion and electron diffusion in electrode materials of LIBs are very important for high rate and high density. To this end, the use of porous materials featuring ordered channel and high surface area has been a successful strategy.

Herein, we reported an easy method of designing S, N-co-doped mesoporous carbon materials with high specific surface area through the carbonization of 2-aminothiazole in molten ZnCl₂. The resultant S,N-co-doped PC (SNPC) material shows high ORR electrocatalytic activity in alkaline media. Furthermore, density functional theory (DFT) calculation results reveal that ORR follows associative mechanism, and the catalytic activity is mainly derived from the synergistic effect of S,N dopants. Moreover, this binary-doped carbon material exhibits good Li-ion battery property.

Experimental

Materials

Anhydrous ZnCl₂ (98%), NiCl₂ (98%), CoCl₂ (97%) and Commercial 20 wt % Pt/C were purchased from Alfa Aesar. 2-Methylimidazole (98%) and 2-Aminothiazole (97%) were acquired from Aladdin. Dibenzothiophene (98%) was obtained from J&K scientific Ltd.. All solvents were obtained from commercial suppliers and used without further purification.

Synthesis of SNPC: SNPC-500, SNPC-600, SNPC-700 and SNPC-800 were obtained under the same procedure except the reaction temperature. A typical experiment for SNPC-500 was presented as follow: A sandwich-like mixture of ZnCl₂ (0.8815g), 2-Aminothiazole (0.1282g) and ZnCl₂ (0.8815g) was placed into the ceramic crucible. Subsequently, the mixture was put in a chamber oven with the exposure of a nitrogen flow (30 ml.min⁻¹) at room temperature for 30 min, and then heat treated at 500 °C for 8 hours under N₂ atmosphere, with ramp rate of 5 °C.min⁻¹. The resultant black powder was extensively washed using a 35% concentration of hydrochloric acid to remove the residual Zn-contained component. Next, the sample was washed several times with deionized water and absolute ethanol, and dried in an oven for 3 h at 80 °C. Finally, the products were further heated to 200 °C for 2h to remove water and ethanol in the surface. The obtained powder was denoted as SNPC-500. The yield for SNPC-500, SNPC-600, SNPC-700 and SNPC-800 are about 70%, 67%, 71% and 68% (based on 2-Aminothiazole).

Synthesis of single-doped NPC and SPC: In comparison to SNPC-800 material, the only nitrogen-doped NPC-800 and sulphur-doped SPC-800 were prepared using the same procedure as described above for the synthesis of SNPC-800, but using 2-Methylimidazole (0.105g) and Dibenzothiophene (0.2359g) in place of 2-Aminothiazole (0.1282g), respectively.

Structural Characterization

The morphologies of samples and elemental mappings were observed transmission electron microscopy (TEM, Tecnai G2 F30) and scanning electron microscopy (SEM, Hitachi S4700). X-ray powder diffraction (PXRD) patterns were recorded in a Panalytical X-Pert pro diffractometer with Cu-K α radiation. A thermal gravimetric analyzer (SDT Q600, TA Instruments Co.) was applied to identify thermal stability, where samples were heated at a rate of 10°C ·min⁻¹ from room temperature to 800°C in an Ar atmosphere. X-ray photoelectron measurements were conducted on a Kratos AXIS Ultra DLD instruments using 300W Al K α radiation and C 1s peak at 284.5 eV as internal standard. The surfaces area based on the nitrogen adsorption isothermal were recorded in an Surface properties analyzer instrument (3Flex, Micromeritics). Raman spectra were recorded with a Renishaw 2000 model confocal microscopy Raman spectrometer.

Measurement of ORR and LIB property

Electrochemical measurements were performed using a three-electrode electrochemical cell. A Ag/AgCl electrode in saturated KCl aqueous solution and a platinum wire were used as reference and counter electrode, respectively. The electrolyte contains 0.1 M aqueous KOH. The process of loading the catalyst on glassy-carbon working electrode is presented as follows: 1) Glassy carbon (GC) electrodes (4 mm diameter) were polished with a 0.05/0.3 mm alumina slurry, and subsequently rinsed with ultrapure water. 2) 0.2 mL of 5 wt % Nafion aqueous solution was added to 1.8 mL of ethanol (99.7+%), and 2 mg of catalysts were dispersed in the as prepared mixtures by at least 10 min sonication to generate a homogeneous catalyst ink. 3) 10 μ L (10 μ g catalyst, 7.96 \times 10⁻⁵g/cm²) of the suspension was uniformly loaded onto as pretreated glassy carbon electrode and was dried under an infrared lamp. For comparison, 1 mg mL⁻¹ commercially 20 wt % Pt/C was also used, 10 μ L of the 20 wt% Pt/C ink was dipped on a as pre-treated glass carbon electrode. Before ORR measurement, the cell was purged with high purity oxygen for at least 30 min. In order to ensure O₂ saturation during the recording of CVs, a flow of O₂ was maintained over the electrolyte. The temperature of electrochemical measurement was about 22 °C. Cyclic voltammetry (CV) curves were measured at a scanning rate of 10 mV s⁻¹ within the potential range from -1.0 to +0.2 V (vs.Ag/AgCl/V) using a CHI760E electrochemistry working station (Shanghai Chen hua, China).

The RDE linear voltammetry was performed by a CHI760E and RRDE-3A (ALS) from -1.0 and +0.2 V (vs.Ag/AgCl/V) at a scan rate of 100 mV s⁻¹. Rotating disk electrode (RDE) measurement: An Ag/AgCl/KCl (3M) and a Pt sheet were used as reference and the counter electrodes, respectively. And the same amount of the catalyst as CV used was dipped on a rotating glass carbon electrode (4 mm in diameter). The linear sweep voltammograms with a scan rate of 10 mV s⁻¹ at rotating speeds range from 400 to 2025 rpm were recorded in O₂-saturated 0.1 M KOH. The reference of potentials was

converted to the RHE, where the potential difference between Ag/AgCl and RHE is 0.965 V¹⁴.

The LIB properties of NPC-800, SPC-800 and SNPC-800 were evaluated using CR2025 coin-type cells assembled in a glove box under argon atmosphere. The working electrode was fabricated by mixing active materials, conductivity agent (Super P), and polyvinylidene fluoride (PVDF) binder at a weight ratio of 70:15:15 in a N-methyl-2-pyrrolidone (NMP) solvent. In order to identify the effects of Super P on LIB properties, we also conducted reference experiments in the mixture of active materials and PVDF (85: 15). The loading mass of each working electrode was about 3 mg (2-3mg cm⁻²). The lithium foil was used as both counter electrode and reference electrode. A 1 M solution of LiPF₆ in the 1:1 ethylene carbonate (EC) and dimethyl carbonate (DMC) solution was used as the electrolyte with a Celgard membrane (2300) as the separator. The galvanostatical charge (Li⁺ extraction) and discharge (Li⁺ insertion) tests were conducted in the voltage range of 0.0-3.0 V at different current densities using a Battery Testing System at ambient temperature (Shenzhen Neware Battery, China). Cyclic voltammetry (CV) curves were measured at a scanning rate of 0.1 mV s⁻¹ within the potential range of 0.0-3.0 V using a CHI660D electrochemistry working station (Shanghai Chen hua, China). Electrochemical impedance spectroscopy (EIS) measurements were conducted in the tablet of 1.76 mm² × 0.20mm with the frequency ranging from 0.01 to 10⁵ Hz at room temperature by Zahner Zennium electrochemical workstation.

DFT Computational Details

All polarized DFT calculations were carried out using the projector-augmented wave (PAW)¹⁵ method of Blöchl, as implemented in the ab initio VASP program¹⁶. PAW method features the accuracy of augmented plane-wave methods as well as the efficiency of the pseudo-potential approach. The generalized gradient approximation (GGA) with Perdew Burke Ernzerhof (PBE)¹⁷ formalism was used to describe the exchange- correlation (XC) effects. One non-local correlation vdW-DF¹⁸ based on opt88 functional was applied to correct the long-distance dispersion interaction. 3s and 3p electrons of S, 2s and 2p electrons of C, N and O, and 1s electrons of H were explicitly treated as valence electrons. The electron wave function is expanded in plane waves up to a cutoff energy of

450 eV and the integration in Brillouin zone adopts Γ centered 9×9×2 grid, which are verified to be enough accurate in the calculation of total energy. The convergence of SCF was assumed when the energy difference between two adjacent circle is less than 1.0×10⁻⁶ eV. The initial structures of SNPC, O-SNPC, HO-SNPC and HOO-SNPC are fully relaxed until the resultant Hellmann–Feynman force per atom is less than 0.02 eV/Å. The adsorption energy were typically calculated according to the formula: $E_a = E(X\text{-SNPC}) - E(X) - E(\text{SNPC})$ (X= O, OH, OOH). On the assumption of real condition (pH = 0, p = 1 bar, T = 298K), the difference of Gibbs free energy (ΔG) was simplified as this formula: $\Delta G = E_a + \Delta ZPE - T\Delta S - n eU$, where n represents the number of transferring electron in elemental reaction and U is labelled as equilibrium potential. And the difference of zero-point energy (ΔZPE) and the change of entropy ΔS were derived from the DFT calculation of vibrational frequencies and standard table of gas molecules, respectively. Herein, we neglect the temperature dependence of enthalpy, as labelled as $\Delta H(298K) = \Delta H(0K)$. Based on the optimized structure, Spin density and frontier orbitals at Gamma point were calculated by DMol software¹⁹ with PBE¹⁷ method and DNP^{19a} basic set.

Results and discussion

Structural Characterization

The morphology and structure of SNPC, NPC and SPC were examined by scanning electron microscopy (SEM) and transmission electron microscopy (TEM). Within this context,

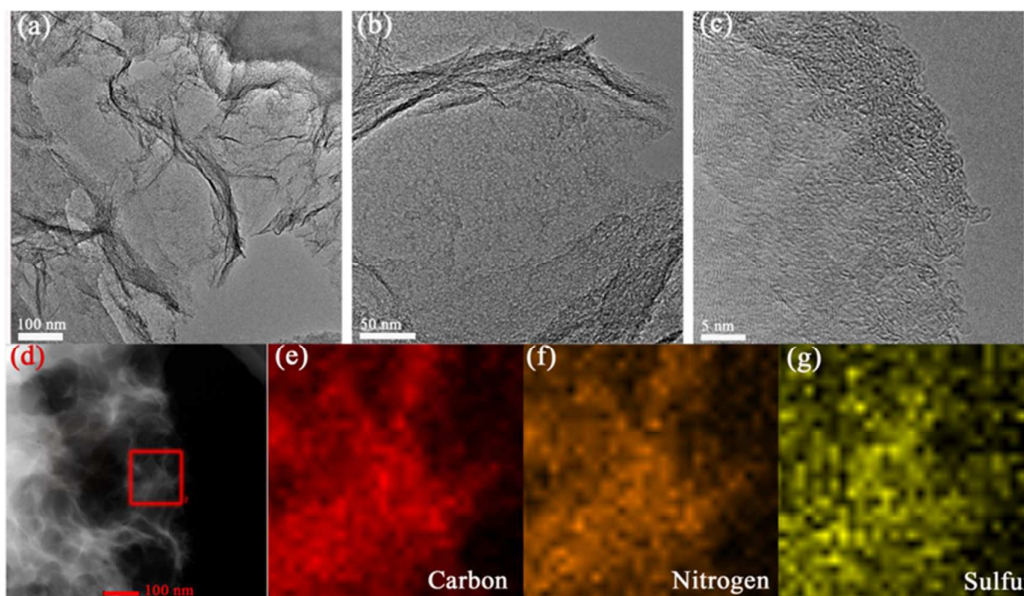


Fig. 1 TEM images of SNPC-800 with a scale bar of 100 nm (a), 50 nm (b), and 5 nm (c). (d–g) EDX maps of SNPC-800, C, N, and S.

SNPC-800 was chosen as a typical example to discuss its morphology and microstructure. The SEM images (Fig. S1) shows hierarchical porous structure of SNPC-800. A distinct fold and cavity of the irregular orientation of graphite layers were identified using low-magnification TEM images (Figs. 1a and 1b). This phenomenon was similar to previously reported results with respect to highly PCs¹⁰ⁱ, indicating the formation of vast graphitized-carbon frameworks. And the high-resolution TEM image (HRTEM) shows that the amorphous carbon materials was formed by the stacking of the curved graphene layers (Fig. 1c). Elemental mapping images revealed that C (red), N (orange), and S (yellow) were uniformly distributed on the entire surface of SNPC-800, as shown in Figs. 1d–1g. Moreover, the morphology and structure of SNPC-500, SNPC-600, and SNPC-700 were similar with SNPC-800 (see Figs. S2–S7). And both SEM and TEM images show NPC-800 hierarchical porous structure and feature multi-layers graphene, as shown in Figs. S8–S9. Meanwhile, we obtained vast sulphur-doped SPC-800 solid carbon microsphere (see Figs. S10–S11), with diameter of about 500 nm, and S (yellow) was uniformly distributed on the entire surface of carbon microsphere.

X-ray diffraction (XRD) patterns of the S,N-co-doped samples, including SNPC-500, SNPC-600, SNPC-700, and SNPC-800, are presented in Fig. 2a. Similar diffraction features with a broad peak at approximately $2\theta = 26^\circ$ corresponded to

the carbon peak (002) of crystal plane. As carbonization temperature increases, the peak at approximately $2\theta = 43^\circ$

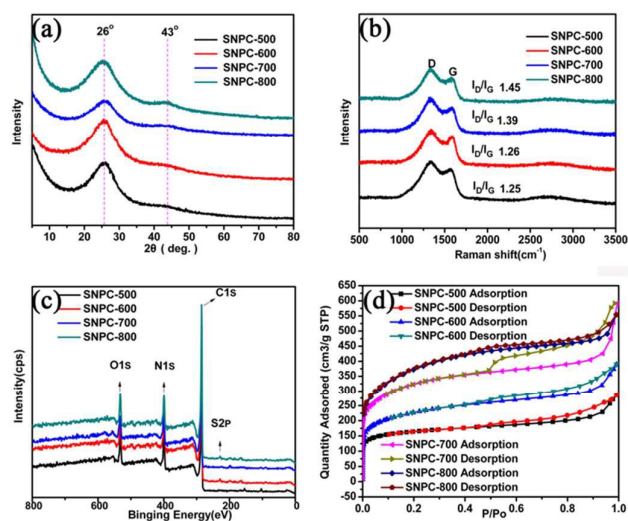


Fig. 2 (a) PXRD curves of the SNPC samples obtained at different carbonization temperatures. (b) Raman spectra of the SNPC samples. (c) Survey XPS spectra of the SNPC samples. (d) Nitrogen adsorption/desorption isotherms of SNPC.

labelled as (100) crystal plane gradually increased, suggesting the ordered degree in the crystal plane improves²⁰. However, the resultant product was ZnS at the carbonization

temperature of 900 °C (see XRD pattern in Fig. S12) because of the full decomposition of organic molecules. To explore the inner structure of SNPC, Raman spectroscopy was also conducted. As displayed in Fig. 2b, Raman spectra showed a disordered band at roughly 1338 cm⁻¹, related to sp³ defects. Moreover, the crystalline band at approximately 1582 cm⁻¹ was attributed to the in-plane vibration of sp² carbon. Notably, the D band was stronger than the G band with I_D/I_G ratio of more than 1.0 for all spectra, implying that a lot of defects exist in SNPC samples. Furthermore, the ratio of I_D/I_G gradually increased from 1.25–1.45 with carbonization temperature increases. This result was due to the fact that the defect of the carbon matrix was prone to be induced at higher temperature. The I_D/I_G ratio for SNPC-800 was greater than that of the other samples, indicating more amount of defect atoms. However, the I_D/I_G ratio for the NPC-800 was only 0.98 (Fig. S13b), suggesting the existence of small amounts of defects, while the I_D/I_G ratio for the SPC-800 was 1.39, implying large amounts of defects in SPC-800 (see Fig. S14b). The elemental analysis (EA) results indicated the C, N, and S contents of SNPC samples, as shown in Table S1. SNPC-700 contained the highest 21.06 wt% nitrogen. However, not all N atoms were incorporated into the graphitic lattice because a high N-doped content could result in structural instability. The N contents at the pyrolysis temperature of 500, 600, and 800 °C were 16.93 wt%, 20.05 wt%, and 14.82 wt%, respectively. With increased pyrolysis temperature, S content gradually increased until reaching the 3.86 wt% sulfur at 800 °C.

Moreover, X-ray photoelectron spectroscopy (XPS) confirmed the component of SNPC, NPC and SPC. As shown in Fig. 2c, the XPS full spectrum showed a dominant C1s peak (284.5 eV), an O1s peak (532.0 eV), an N1s peak (400.0 eV), and a visible S2p peaks (228.0 eV). The existence of an O1s peak in SNPC may be due to the incorporation of adsorbed oxygen and H₂O on the surface of SNPC sample. To further investigate the chemical states of C, N, and S, the high-resolution C1s, N1s, and S2p peaks were identified in detail. The high-resolution spectrum of C1s in SNPC could be divided into five single peaks, corresponding to C–S, C–C, N–C (sp²), N–C (sp³), and S=C, as displayed in Fig. S15. In the high-resolution N1s spectra of SNPC (Fig. S16), the peaks of 398.3, 399.8, 400.9, and 402.5 eV were attributed to pyridinic nitrogen (N1), pyrrolic nitrogen (N2), graphitic nitrogen (N3) and S-N (N4) atoms, respectively. Based on the intensity of XPS (Fig. S17a and b), the N-binding configuration included 38.77% N1, 43.25% N2, 13.82% N3, and 4.36% N4 for SNPC-800. Notably, with increased temperature from 500–800 °C, the S2p peaks gradually increased. To verify the experimental reproducibility, we repeated the high-resolution S2p XPS spectra of the re-produced SNPC sample and gained the same results. As shown in Fig. S18, the S2p peaks can be resolved to three different peaks: both of two peaks at 163.82 eV (165 eV, S1) and 166.92 eV (168.1 eV, S2) can be assigned to the S atoms in the moieties of C–S and C=S, and the peak at 168.22 eV (169.4 eV, S3) is attributed to the S atoms of N–S bonds. S atoms had been successfully doped into carbon matrix by the current method. In comparison to SNPC samples, high

resolution N1s XPS spectra of NPC-800 and S2p XPS spectra of SPC-800 (see Figs. S19 - S20) indicates the only nitrogen-doped NPC-800 and sulphur-doped SPC-800. In addition, this result coincided well with the C1s peak. Therefore, the heteroatom modifications in the pristine graphite plane can render more defects than those in the perfect ones, which is beneficial for the charge transfer.

The porosity of SNPC, NPC and SPC were further confirmed by N₂ adsorption experiment at 77.3 K, resulting in the parameters of specific surface area, pore size, and pore volume (see Fig. 2d). Scrutinizing the N₂ adsorption–desorption isotherms showed that the distinct hysteresis loop characteristic at the P/P₀ of more than 0.40 was found in the four SNPC samples. Based on the definition criterion of International Union of Pure and Applied Chemistry (IUPAC), SNPC materials feature the mesoporous property. Specific surface area is typically calculated by Brunauer–Emmett–Teller method. SNPC-800 had higher specific surface area (1235 m²/g) than SNPC-700 (1173 m²/g), SNPC-600 (821 m²/g) and SNPC-500 (622 m²/g). With increased S content, specific surface area also improved. Pore-size distributions calculated by Barrett–Joyner–Halenda method showed that the pores of SNPC-800 material are distributed in the scale of 10–45 nm (see Fig. S21), which is considerably larger than those obtained through carbonization of ionic-liquid¹⁰ⁱ, and fabrication of graphene oxides^{10c}. Notably, the higher specific surface area and broad pore-size distribution were mainly beneficial for the transfer of reaction substrate, thereby reducing the energy barrier of diffusion. Moreover, no hysteresis loop was observed in the N₂ adsorption/desorption isotherms of NPC-800, as shown in Fig. S13d, suggesting the microporous trait, while SPC-800 with hysteresis loop above P/P₀ of 0.60 shows mesoporous characteristic (see Fig. S14d). Furthermore, the specific surface area of NPC (1195 m²/g) SPC-800 (315 m²/g) was smaller than that of SNPC. Thermogravimetric properties were also performed in an argon atmosphere at a heating rate of 10 °C/min⁻¹, indicating thermostability improved with increased carbonization temperature (see Fig. S22). Notably, SNPC-800 exhibited greater thermostability than pristine graphene.

Generally, N-doped, S-doped and S, N-co doped porous carbon materials were successfully synthesized by one-spot method. In this vein, ZnCl₂ acts as good solvent of C, N-containing monomers as well as Lewis catalyst for the reaction. In order to uncover the role of ZnCl₂, we conducted reference experiments using the same procedure as described above, but using CoCl₂ and NiCl₂ in space of ZnCl₂, respectively. However, the final products are not black porous carbon but Co/Ni-containing compounds (see Fig. S33). Therefore, it is found that molten ZnCl₂ play a critical role in the preparation of porous material.

ORR properties

To evaluate ORR catalytic activity, we performed cyclic voltammetry (CV) measurements of SNPC, NPC and SPC in O₂-saturated 0.1 M KOH electrolyte solutions at a constant active mass loading and a scan rate of 10 mV s⁻¹. NPC-800 and SPC-

800 material exhibited modest cathodic ORR peak (0.51 V for SPC-800, 0.41 V for NPC-800) with a current density of $-0.92 \text{ mA}\cdot\text{cm}^{-2}$ for SPC-800 and $-1.2 \text{ mA}\cdot\text{cm}^{-2}$ for NPC-800. Noticeably, SNPC-800 showed an ORR peak at the most positive potential (0.63 V), onset potential (0.86 V), and higher current density($-2.1 \text{ mA}\cdot\text{cm}^{-2}$) among all electrodes (Fig. 3a). And electrocatalytic activities of SNPC improve with increased carbonization temperature. The superior ORR activity in SNPC-800 hybrid can be concluded as three aspects. Firstly, the ORR performance of SNPC-800 highly depended on the content and types of doped nitrogen. According to XPS and EA results, SNPC-800 has the most content of N1 and N2 in spite of low total-nitrogen amount. These N atoms doped in PC matrix is likely to trigger charge density on the C atoms because of the larger difference in the electronegativity between N and C atoms^{4b}. The resultant charge separation promotes the adsorption of O_2 over catalyst and hence improves ORR property. Secondly, doping sulfur atoms are not active site of ORR, due to less difference of electronegativity between C and S atom. However, these S atoms, featuring two-pair local electron and larger atomic radius (110 pm) than C (70 pm) and N (65 pm) atoms, can easily induce the

($1.10 \times 10^{-2} \sigma / \text{cm}^2$) and SPC-800 ($8.60 \times 10^{-3} \sigma / \text{cm}^2$), as shown in Fig. S. Therefore, catalytic activity of SNPC is much better than N-doped²¹ and S-doped mesoporous carbons^{9b}. In conclusion, the excellent ORR activity of SNPC-800 was due to the synergistic effect of N, S, and the mesoporous structure.

To gain further insight into the ORR process on SNPC-800 and NPC-800 catalysts, linear sweep voltammetry (LSV) measurements were conducted on a rotating-disk electrode (RDE) at different rotating speeds from 400–2025 rpm. Fig. S23a shows that the current density of SNPC-800 increases as the rotating rate increases, which is caused by the enhanced diffusion of electrolytes. ORR onset potentials of each sample were acquired from RDE LSV at 1600 rpm, as displayed in Fig. 3b. Evidently, SNPC-800 significantly showed better performance than the 20 wt% Pt/C and other SNPC samples in both onset potential and reaction current density. These results indicated that N and S dual doping in our case was very effective for ORR activity enhancement, and the possible reason was that the dual doping can create larger numbers of active sites toward ORRs. The Koutechy–Levich plots ($\text{J}^{-1} \text{ mA cm}^{-2}$) of all samples were resolved from LSVs for different potentials (Figs. 3c and S23b). The obtained plots showed fairly good linear relations, hinting first-order reaction kinetics toward dissolved oxygen and similar electron transfer number for the ORR process at different potentials. Furthermore, SNPC-800 showed high ORR current, which was surprisingly insignificantly superior to NPC-800 and approached that of Pt/C. The transferred electron numbers (n) (Fig. S23c) per oxygen molecule involved in the ORR process can be identified based on Koutechy–Levich equations. The electron number of $n = 2.2, 2.3$ and 4.2 were responsible for NPC-800, SPC-800 and Pt/C, respectively. The obtained electron number n for SNPC-800 was 4.1 at -0.6 V (vs.Ag/AgCl/V), indicating that SNPC-800 electrode follows a four-electron mechanism. This result is good agreement with those reported previously^{4b, 22}.

An ORR electrocatalyst for fuel cells should have high catalytic selectivity for cathode reactions against fuel oxidation, especially when using small-molecule organic fuels such as methanol. These organic fuels can easily penetrate through a polymer electrolyte membrane from the anode to cathode, thereby compromising cell performance. Fig. S23d shows that the ORR current for SNPC-800 remained unchanged, whereas that for Pt/C sharply decreased after adding 3 M methanol to a 0.1 M KOH solution saturated with O_2 . This result indicated that SNPC-800 had high stability and immunity toward methanol crossover in addition to its excellent electrocatalytic activity. The durability of SNPC-800 and Pt/C was also evaluated through chronoamperometric measurements at -0.2 V in O_2 -saturated 0.1M KOH solution for 2000 cycles (Fig. 3d). Evidently, SNPC-800 exhibited a high relative current of 87% that still persisted after 2000 cycles. By contrast, Pt/C showed a gradual decrease with a current loss of approximately 30% measured after 2000 cycles. The CV curves of the ORR before and after 2000 cycles for SNPC-800 and Pt/C (Fig. 3e) further confirmed that SNPC-800 exhibits better stable performance than Pt/C for ORR. Overall, SNPC-800 showed good ORR catalytic stability.

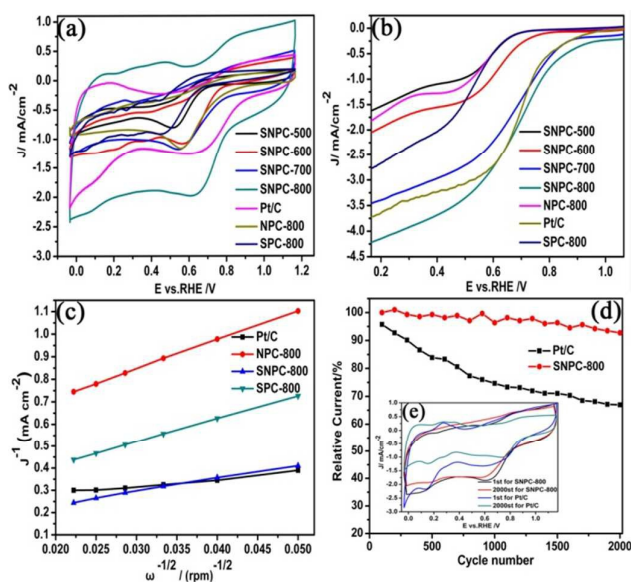


Fig. 3 (a) CV curves of the samples in O_2 -saturated 0.1 M KOH; (b) LSV curves of the samples on an RDE (1600 rpm) in an O_2 -saturated 0.1M KOH solution; (c) Koutechy–Levich plots of the samples at -0.6 V (vs.Ag/AgCl/V); (d) endurance test of the samples for 2000 cycles in 0.1 M KOH. (e) The 1st and 2000th cycle voltammetry curves of the samples in aqueous 0.1 M KOH saturated with O_2 .

polarization neighboring of C and N atoms, resulting in strain and defect in carbon framework. These defects usually serve as adsorption sites of substrate in ORR⁸. This improvement was evidently concluded by comparison with NPC-800 and SPC-800. Third, N, S-doped atoms affected the electronic structure of carbon materials, resulting in the increases of conductivity and electrochemical activity. This point can be confirmed by the fact that the conductivity of SNPC-800($1.62 \times 10^{-2} \sigma / \text{cm}^2$) is larger than those of NPC-800

Generally, SNPC-800 exhibited comparable ORR activity and better stability than commercial Pt/C catalyst in 0.10 M KOH solution, making it one of the best-performing metal-free carbon ORR catalysts. The durability of SNPC-800 was superior to that of the Pt/C catalyst. Furthermore, from the view of practical application, this feature is particularly important.

LIB properties

Moreover, we evaluated the LIB properties of NPC-800, SPC-800 and SNPC-800 by assembling CR2025 coin type cells, where three samples acted as the anode materials of LIBs, as shown in Fig. 4 and Figs S27-S31. All specific capacities had been calculated on the total mass of the composites. Fig. S27a shows the CV curves of SNPC-800 electrode at room temperature between 0.0 and 3.0 V at a scanning rate of 0.1 mV s⁻¹. Compared with the other cycle, the first discharge cycle with large inevitable capacities below 1V can be ascribed to the formation of solid electrolyte interface (SEI) layers because of the side reactions on the electrode surfaces and interfaces. From the second cycle onwards, the CV curves almost overlapped, indicating the stable and superior reversibility of SNPC. The charge/discharge profiles of SNPC-800 sample at a current density of 0.1 A g⁻¹ between 0 and 3 V are displayed in Fig. S27b. The first discharge and charge capacities of SNPC-800 sample were 1340.66 and 678.35 mAh

g⁻¹, respectively. The large capacity loss in the first cycle was mainly attributed to the irreversible processes such as inevitable formation of the SEI layer²³. The initial discharge curve had a long slope, which can be assigned to the formation of the SEI film and the insertion of Li⁺ ions into carbon material. The phenomenon was consistent with the previous CV curves. Slow shrinkage of the charge/discharge curves after the first cycle demonstrated good cycling stability. Meanwhile, from the second cycle onward, SNPC-800 electrode showed the fascinating cycling stability (Fig. 4a). The Coulombic efficiency steadily reached around 99% accompanied by the increasing cycle number, indicating highly efficient Li⁺ ion-insertion/extraction. Among the working anodes, the NPC-800 anode showed the lower capacity and decreased after 50 cycles, whereas SNPC-800 anode exhibited the higher electrochemical performance with enhanced capacity retention. At the end of the 50th cycle, a reversible capacity as high as 675.1 mAh g⁻¹ can be retained for SNPC-800, whereas NPC-800 and commercial graphite can deliver a specific capacity of only 329.1 and 372 mAh g⁻¹, respectively. Moreover, with increased current density from 0.1–1 A g⁻¹, the discharge and charge capacities remained stable and regularly decreased with an enhanced rate (Fig. 4b). The corresponding reversible

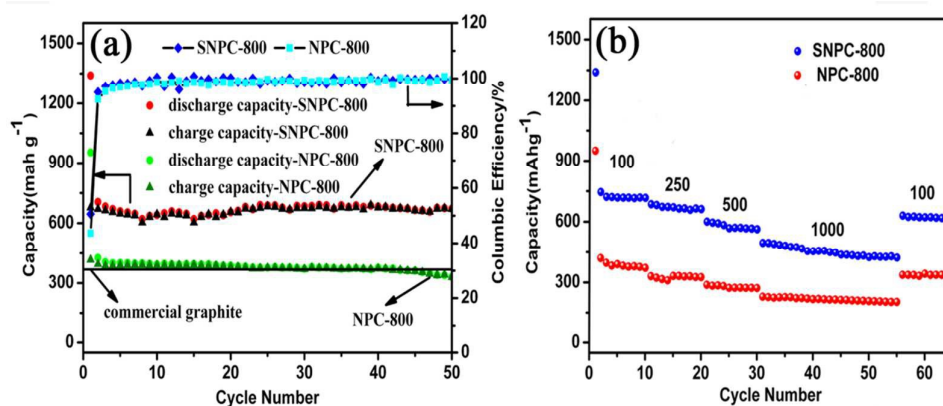


Fig. 4. LIB properties of the as-prepared samples. (a) Cycling performance and Coulombic efficiency of samples SNPC-800 and NPC-800 at a 100 mA g⁻¹ current density. (b) Rate performance of samples SNPC-800 and NPC-800 (current density unit: mA g⁻¹).

capacities at 0.1, 0.25, 0.5, and 1 A g⁻¹ were 720.2, 671.3, 570.6, and 467.5 mAh g⁻¹, respectively. This phenomenon was mainly due to the kinetic-limited effects of the electrochemical conversion reaction in nature, rendering a higher overpotential and a lower capacity at a higher current. Furthermore, the capacity rapidly remained at 630.5 mAh g⁻¹ and retains excellent stability after another 55 cycles upon reducing the rate to 0.1 A g⁻¹. Noticeably, the reversible capacities of SNPC-800 anodes were always higher than NPC-800 and SPC-800 anodes, and they all had excellent cycling stability (see Fig. S27). In order to identify the effect of conductivity agent (Super P) on the LIB property, we also conducted parallel experiments without conductivity agent, as shown in Figs. S28-S31. The first discharge and charge capacities of SNPC-800 sample were 1473.28 and 828.73 mAh g⁻¹ (Fig. S28), respectively, where the higher capacities can be attributed to

extra 15% more active component of SNPC-800 than that of preceding experiment with Super P. Meanwhile, the specific capacities of NPC-800 and SPC-800 after 25 cycle are 360.37 and 385.82 mAh g⁻¹, which is smaller than that of SNPC-800. In this regard, this result generally demonstrates the effect of Super P on the capacity is very small.

The good lithium-ion storage performance of SNPC-800 was due to the S, N-co-doping, novel structure, and high degree of graphitization. The porous networks, high specific surface areas, and large numbers of pores provided a large space that served as the reservoir for the storage of Li⁺ ions and reduced the diffusion length of Li⁺ ions. Moreover, the stability of PC guaranteed the sustainable cycles. By contrast, N, S-co-doping simultaneously improved the conductivity and the electrochemical activity of SNPC-800, which can generate high capacity. Notably, high N²⁴ and S²⁵ contents in PC contributed

to a high specific capacity for Li storage, and their sites can attract more Li^+ ions and adjust the electron properties of the adjoining carbon atoms with the cycles. Therefore, SNPC sheets of SNPC-800 can accept a greater charge than the commercial graphite, SPC-800 and NPC-800.

DFT calculation for ORR Mechanism

To determine the ORR catalytic mechanisms, spin-polarized DFT calculations for SNPC-800 were conducted. Based on XPS, EA, and TEM results, the accurate structure of SNPC-800 was difficult to be determined. The real model must consider the arrangement of various N, S, and C components, leading to a large number of possible configurations. Therefore, we had to simplify the model of SNPC as graphitic N, S, and C atoms. Essentially, the electronic effect of S atom on graphitic N was similar to those of pyridinic nitrogen and pyrrolic nitrogen. In view of the C, N, and S ratio of 25:5:1 obtained by EA results, the initial geometry can be derived from the doping of 10 N

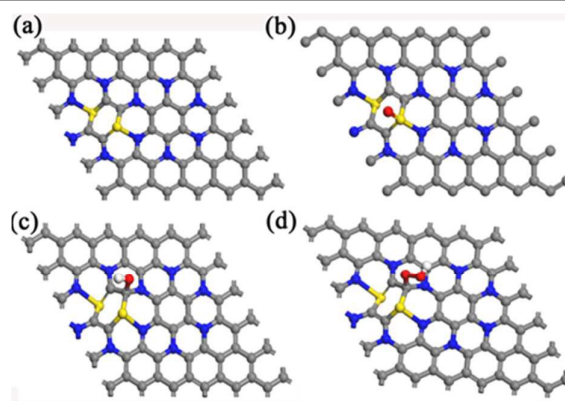


Fig. 5. Most stable structures of SNPC (a), O-SNPC (b), OH-SNPC (c), and OOH-SNPC (d)

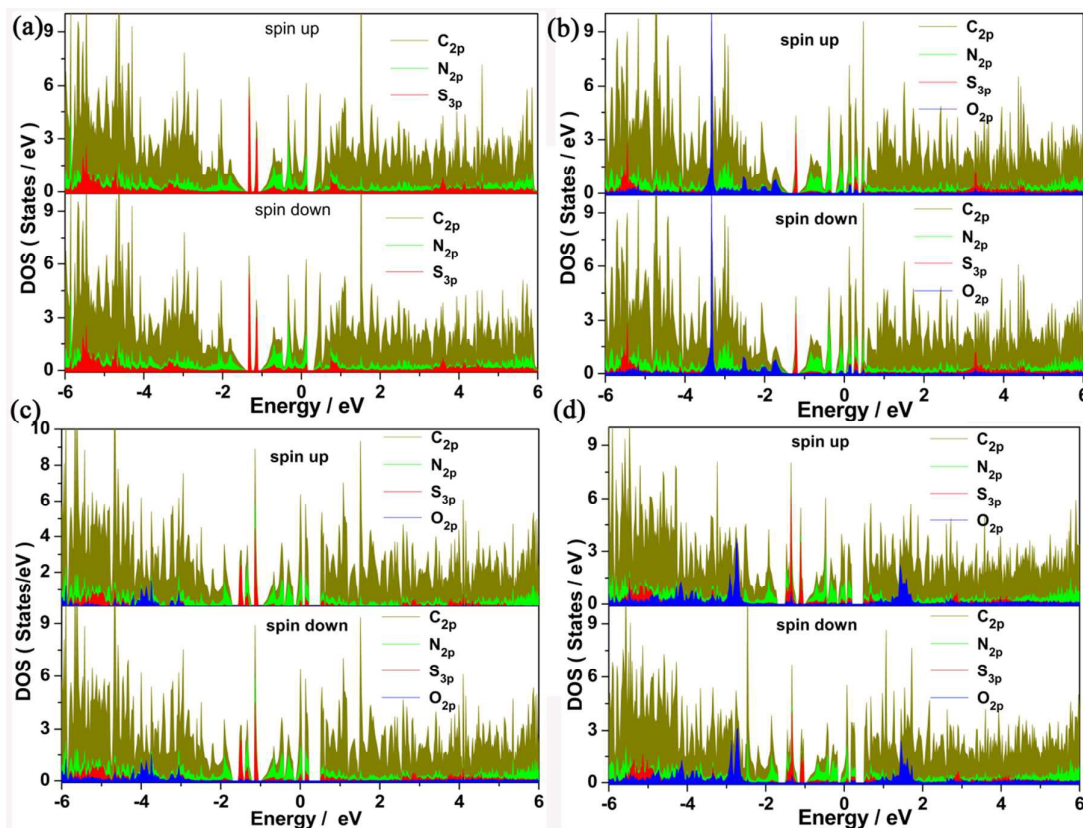


Fig. 6. Partial DOS of SNPC (a), O-SNPC (b), OH-SNPC (c), and OOH-SNPC (d) with the Fermi level of 0.0 eV relative energy.

atoms and 2 S atoms on the surface of 6×7 super cell graphene. Geometrical optimization of SNPC was summarized as the following three steps. First, 6×7 super cell graphene was fully relaxed without any constraint. Second, the most stable structure of ten N-doped graphene was resolved by step by step. N doping prefers the para-position of graphene. Finally, we searched the most stable structure of the two S doping on N ten N-doped graphene (Fig. 5a), where the S atoms are lifted away from the surface of graphene. Through

the consideration of all possible adsorption sites and initial configurations, the adsorption properties of the three key intermediates consisting of O, OH, and OOH were further identified. As shown in Figs. 5b–5d, O preferred to be adsorbed on S atom, whereas the preferred adsorption sites for OH and OOH were the C atom around S atoms. The adsorption energies were -1.39 , -2.89 , and -1.27 eV for O, OH, and OOH, respectively. O, OH, and OOH had stronger adsorption on SNPC. Scrutinizing Bader charge results revealed

that after substrate adsorption, the atomic charge around adsorption sites significantly changed. For the case of O-SNPC, the O component endowed 1.17 electrons to S1 atoms, whereas OH and OOH had 0.41 and 0.35 e from bonding C2 atom (see Table S2), respectively. Noticeably, chemical bonds were produced between substrates and SNPC. Thus, the spin density of SNPC was distributed on the S atom and adjacent to C and N atoms (as shown Fig. S32a), leading to the significant enhancement of ORR catalytic activity. This conclusion is also in line with that reported by Qiao^{10b}. The frontier orbital figure of SNPC (see Figs. S32b–d) revealed that the highest occupied molecular orbitals (HOMO), lowest unoccupied molecular orbitals(LUMO), and HOMO-1 concentrate on the 3p-dialing orbitals of S, 2p-localized orbitals of N, and O near S atoms. Hence, it is directly observed that S, N- doping atoms can act as synergistic sites in ORR.

To examine the electronic effect of S and N atoms on SNPC, partial density of states (PDOS) were further calculated for pristine SNPC and O, OH, OOH-adsorbed SNPC, as shown in Fig. 6. After inspecting the four PDOS, we can conclude four important points. First, no noticeable differences exist between the states of spin up and spin down, implying weak stronger spin polarizations on the most stable structure. Second, the overlapping of PDOS between O and SNPC validated stronger adsorption of the three key intermediates. Third, for the case of SNPC, 2p PDOS of N, 3p PDOS of S, and 2p PDOS of C dispersed well in the vicinity of Fermi level, resulting in effective overlap among them. This result enabled synergistic catalysis. Fourth and last, for OH-SNPC and OOH-SNPC with the C adsorption sites, the two main peaks of S PDOS at -1.3 eV below the Fermi level showed a characteristic similar to that of pure SNPC (Figs. 6a, 6b, and 6d), whereas only one main peak existed at the same position for the O-SNPC with the S adsorption site, as shown in Fig. 6b. The phenomenon can be due to the fact that upon adsorption of O* moiety to S1, the obtained electrons of S1 can transfer to S2 and thereby produced a degenerate state, as confirmed by the results of Bader charge. In conclusion, both S atoms can also generate synergistic effect. Xia et al. indicated that the Stone–Wales defect of S-doped graphene plays an important role in the catalytic activity of ORR⁸. However, our calculation results showed that no such defect existed in SNPC, and that ORR performance can result from synergistic electronic effects among N and S atoms from the view of PDOS.

Gibbs free-energy diagrams for ORR on SNPC can help obtain quantitative information of reaction kinetics. In N-doped graphene, Hu et al. found that ORR showed two different mechanisms²⁶, i.e., dissociative and associative mechanisms, which involve five and three elemental steps, respectively. The largest difference between them is whether the OOH* moiety is produced on the catalyst. In the present

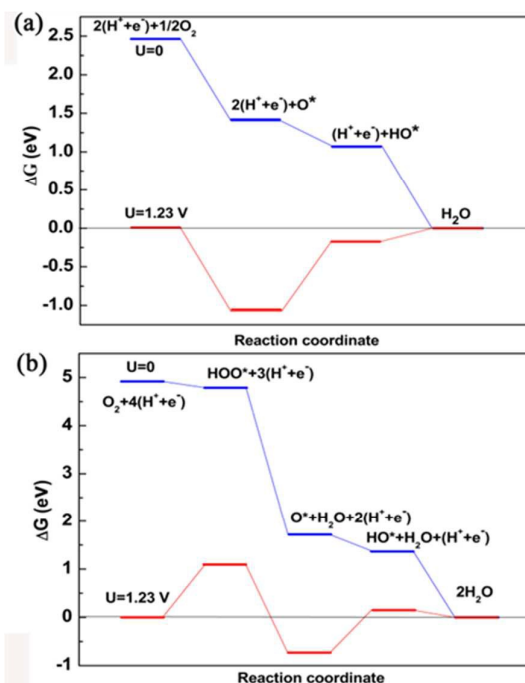


Fig. 7 Diagram of free energy at $U = 0$ and 1.23 V for SNPC under two different mechanisms: dissociative (a) and associative mechanisms (b).

work, we calculated their Gibbs free-energy diagrams at the equilibrium potential of 0 and 1.23 V, as displayed in Fig. 7. Noticeably, the rate-determining steps were the formation of OOH for associative mechanism and the formation of HO* for dissociative mechanism. The reaction barriers, calculated by the difference in Gibbs free energy between intermediates, were 1.08 and 0.92 eV for associative and dissociative mechanisms, respectively. However, for dissociative mechanism, the uphill of 0.15 eV continued to appear in H₂O formation, resulting in the required energy of 1.07 eV. For associative mechanism, the formations of O* and H₂O were exothermic reactions with released energies of 1.82 and 0.15 eV, respectively. Therefore, ORR on SNPC preferred associative mechanism, which well agreed with experimental results.

Conclusions

We successfully designed a novel and efficient method of synthesizing S,N-co-doped mesoporous carbon material, where molten ZnCl₂ served as solvent and catalyst. This method was simple, green, and able to produce high yield. The resultant SNPC material exhibited higher ORR performance, stability, and methanol tolerance than commercial Pt/C electrocatalyst. SNPC also showed good LIB property. DFT calculations demonstrated that ORR catalytic activity was due to the synergistic effect of S,N dopants through an associative mechanism. Therefore, this study presented a highly promising metal-free electrocatalyst for alkaline fuel cells and anode materials for LIBs. This new method of designing dual- or multi-heteroatom-doped catalysts can serve as a general strategy for synthesizing other carbon materials.

Acknowledgements

This work was supported by the 973 project (2013CB733501), the National Natural Science Foundation of China (21136001, 21176221, 21306169 and 91334013), Zhejiang Provincial Natural Science Foundation of China (No: LY15B010005) and Zhejiang Provincial Education Department Research Program (No Y201326554).

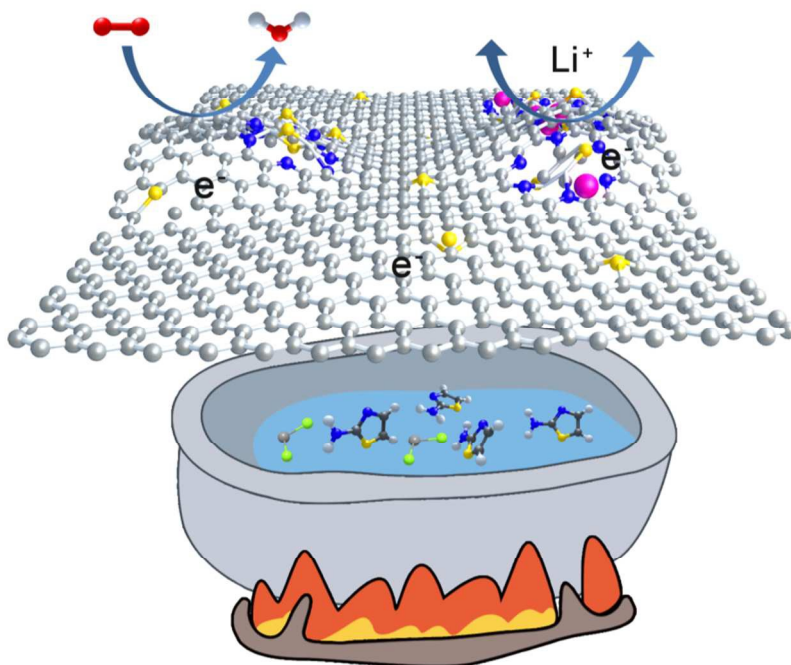
Notes and references

- H. A. Gasteiger and N. M. Markovic, *Science*, 2009, **324**, 48-49.
- (a)D. S. Su and G. Sun, *Angew. Chem., Int. Ed.*, 2011, **50**, 11570-11572; (b)Y. Bing, H. Liu, L. Zhang, D. Ghosh and J. Zhang, *Chem. Soc. Rev.*, 2010, **39**, 2184-2202; (c)Z. Chen, D. Higgins, A. Yu, L. Zhang and J. Zhang, *Energy Environ. Sci.*, 2011, **4**, 3167-3192; (d)X. Huang, Z. Zhao, L. Cao, Y. Chen, E. Zhu, Z. Lin, M. Li, A. Yan, A. Zettl, Y. M. Wang, X. Duan, T. Mueller and Y. Huang, *Science*, 2015, **348**, 1230-1234.
- (a)H. A. Gasteiger, S. S. Kocha, B. Sompalli and F. T. Wagner, *Applied Catalysis B: Environmental*, 2005, **56**, 9-35; (b)F. A. de Bruijn, V. A. T. Dam and G. J. M. Janssen, *Fuel Cells*, 2008, **8**, 3-22; (c)Greeley, J. I. E. L. Stephens, A. S. Bondarenko, T. P. Johansson, H. A. Hansen, T. F. Jaramillo, Rossmeisl, Chorkendorff and J. K. Nørskov, *Nat Chem*, 2009, **1**, 552-556; (d)J. K. Nørskov, T. Bligaard, J. Rossmeisl and C. H. Christensen, *Nat Chem*, 2009, **1**, 37-46.
- (a)X. Zhong, H. Yu, X. Wang, L. Liu, Y. Jiang, L. Wang, G. Zhuang, Y. Chu, X. Li and J.-g. Wang, *ACS Appl. Mater. Interfaces*, 2014, **6**, 13448-13454; (b)S. Bag, B. Mondal, A. K. Das and C. R. Raj, *Electrochim. Acta*, 2015, **163**, 16-23.
- (a)S. Guo, S. Zhang and S. Sun, *Angew. Chem., Int. Ed.*, 2013, **52**, 8526-8544; (b)J. Jin, F. Pan, L. Jiang, X. Fu, A. Liang, Z. Wei, J. Zhang and G. Sun, *ACS Nano*, 2014, **8**, 3313-3321; (c)G. Wu, N. H. Mack, W. Gao, S. Ma, R. Zhong, J. Han, J. K. Baldwin and P. Zelenay, *ACS Nano*, 2012, **6**, 9764-9776; (d)T. Xing, Y. Zheng, L. H. Li, B. C. C. Cowie, D. Gunzelmann, S. Z. Qiao, S. Huang and Y. Chen, *ACS Nano*, 2014, **8**, 6856-6862.
- R. Jasinski, *Nature*, 1964, **201**, 1212-1213.
- (a)Z. Li, G. Li, L. Jiang, J. Li, G. Sun, C. Xia and F. Li, *Angew. Chem., Int. Ed.*, 2015, **54**, 1494-1498; (b)S. Wang, E. Iyyamperumal, A. Roy, Y. Xue, D. Yu and L. Dai, *Angew. Chem. Int. Ed.*, 2011, **50**, 11756-11760; (c)W. Yang, T.-P. Fellinger and M. Antonietti, *J. Am. Chem. Soc.*, 2011, **133**, 206-209.
- L. Zhang, J. Niu, M. Li and Z. Xia, *J. Phys. Chem. C*, 2014, **118**, 3545-3553.
- (a)Z. Yang, Z. Yao, G. Li, G. Fang, H. Nie, Z. Liu, X. Zhou, X. a. Chen and S. Huang, *ACS Nano*, 2012, **6**, 205-211; (b)H. Wang, X. Bo, Y. Zhang and L. Guo, *Electrochim. Acta*, 2013, **108**, 404-411.
- (a)Y. Ito, W. Cong, T. Fujita, Z. Tang and M. Chen, *Angew. Chem. Int. Ed.*, 2015, **54**, 2131-2136; (b)J. Liang, Y. Jiao, M. Jaroniec and S. Z. Qiao, *Angew. Chem. Int. Ed.*, 2012, **51**, 11496-11500; (c)J. Xu, G. Dong, C. Jin, M. Huang and L. Guan, *ChemSusChem*, 2013, **6**, 493-499; (d)C. Dominguez, F. J. Perez-Alonso, S. A. Al-Thabaiti, S. Nassir Basahel, A. Y. Obaid, A. Obaid Alyoubi, J. L. Gomez de la Fuente and S. Rojas, *Electrochim. Acta*, 2015, **157**, 158-165; (e)W. Li, D. Yang, H. Chen, Y. Gao and H. Li, *Electrochim. Acta*, 2015, **165**, 191-197; (f)J. Shi, X. Zhou, P. Xu, J. Qiao, Z. Chen and Y. Liu, *Electrochim. Acta*, 2014, **145**, 259-269; (g)Y. Li, H. Zhang, Y. Wang, P. Liu, H. Yang, X. Yao, D. Wang, Z. Tang and H. Zhao, *Energy Environ. Sci.*, 2014, **7**, 3720-3726; (h)Y. Jung-Min, M. S. Ahmed, H. Hyoung Soon, C. Ju Eun, Z. Ustundag and J. Seungwon, *J. Power Sources*, 2015, **275**, 73-79; (i)W. Yang, X. Yue, X. Liu, J. Zhai and J. Jia, *Nanoscale*, 2015, **7**, 11956-11961.
- P. Kuhn, M. Antonietti and A. Thomas, *Angew. Chem., Int. Ed.*, 2008, **47**, 3450-3453.
- (a)X. W. Lou, L. A. Archer and Z. Yang, *Adv. Mater.*, 2008, **20**, 3987-4019; (b)Z. Wang, L. Zhou and X. W. Lou, *Adv. Mater.*, 2012, **24**, 1903-1911; (c)Y. Yang, G. Zheng and Y. Cui, *Chem. Soc. Rev.*, 2013, **42**, 3018-3032; (d)X. Xia, Y. Zhang, D. Chao, C. Guan, Y. Zhang, L. Li, X. Ge, I. M. Bacho, J. Tu and H. J. Fan, *Nanoscale*, 2014, **6**, 5008-5048; (e)C. K. Chan, H. Peng, G. Liu, K. McIlwrath, X. F. Zhang, R. A. Huggins and Y. Cui, *Nat. Nanotechnol.*, 2008, **3**, 31-35.
- (a)L. Yu, Z. Wang, L. Zhang, H. B. Wu and X. W. Lou, *J. Mater. Chem. A*, 2013, **1**, 122-127; (b)L. Shen, L. Yu, H. B. Wu, X.-Y. Yu, X. Zhang and X. W. Lou, *Nat. Commun.*, 2015, **6**, 6694-6701.
- H.-W. Liang, X. Zhuang, S. Brüller, X. Feng and K. Müllen, *Nature communications*, 2014, **5**, 4973.
- P. E. Blohl, *Physical Review B*, 1994, **50**, 17953.
- (a)G. Kresse and J. Furthmüller, *Computational Materials Science*, 1996, **6**, 15-50; (b)G. Kresse and J. Hafner, *Physical Review B*, 1993, **47**, 558-561.
- J. P. Perdew, K. Burke and M. Ernzerhof, *Phys. Rev. Lett.*, 1996, **77**, 3865-3868.
- J. Klimeš, D. R. Bowler and A. Michaelides, *Physical Review B*, 2011, **83**, 195131.
- (a)B. Delley, *J. Chem. Phys.*, 1990, **92**, 508-517; (b)B. Delley, *J. Chem. Phys.*, 2000, **113**, 7756-7764.
- G. Wang, J. Yang, J. Park, X. Gou, B. Wang, H. Liu and J. Yao, *J. Phys. Chem. C*, 2008, **112**, 8192-8195.
- R. Silva, D. Voiry, M. Chhowalla and T. Asefa, *J. Am. Chem. Soc.*, 2013, **135**, 7823-7826.
- (a)Y. She, Z. Lu, M. Ni, L. Li and M. K. H. Leung, *ACS Appl. Mater. Interfaces*, 2015, **7**, 7214-7221; (b)S. Yuezeng, Z. Yi, Z. Xiaodong, L. Shuang, W. Dongqing, Z. Fan and F. Xinliang, *Carbon*, 2013, **62**, 296-301.
- (a)X. Y. Tao, R. Wu, Y. Xia, H. Huang, W. C. Chai, T. Feng, Y. P. Gan and W. K. Zhang, *ACS Appl. Mater. Interfaces*, 2014, **6**, 3696-3702; (b)Y. Xia, Z. Xiao, X. Dou, H. Huang, X. H. Lu, R. J. Yan, Y. P. Gan, W. J. Zhu, J. P. Tu, W. K. Zhang and X. Y. Tao, *ACS Nano*, 2013, **7**, 7083-7092.
- F. Zheng, Y. Yang and Q. Chen, *Nature communications*, 2014, **5**.
- D. Sun, J. Yang and X. Yan, *Chem. Commun.*, 2015, **51**, 2134-2137.
- L. Yu, X. Pan, X. Cao, P. Hu and X. Bao, *J. Catal.*, 2011, **282**, 183-190.

Synergistic effect of S,N-co-doped Mesoporous Carbon Materials with High Performance for Oxygen-Reduction Reaction and Li-ion batteries

Gui-lin Zhuang,^{†,‡} Jia-qi Bai,^{†,‡} Xin-yong Tao,^{‡,‡} Jian-min Luo,[‡] Xin-de Wang,[†] Yi-fen Gao,[†]

Xing Zhong,[†] Xiao-nian Li,[†] Jian-guo Wang^{*†}



We reported a new and efficient method of synthesizing S,N-co-doped mesoporous carbon material, which exhibit high performance for ORR and LIB properties.